Monthly Notices
of the
ROYAL ASTRONOMICAL SOCIETY

MNRAS **431,** 1405–1416 (2013)
Advance Access publication 2013 March 5

doi:10.1093/mnras/stt263

Multicolour–metallicity relations from globular clusters in NGC 4486 (M87)★

Juan C. Forte,[1,2†] Favio R. Faifer,[2,3,4] E. Irene Vega,[2,3] Lilia P. Bassino,[2,3,4] Analía V. Smith Castelli,[2,3,4] Sergio A. Cellone[2,3,4] and Douglas Geisler[5]

[1]*Planetario 'Galileo Galilei', Secretaría de Cultura, Ciudad Autónoma de Buenos Aires, Argentina*
[2]*Consejo Nacional de Investigaciones Científicas y Técnicas, Av. Rivadavia 1917, C1033AAJ, Ciudad Autónoma de Buenos Aires, Argentina*
[3]*Facultad de Ciencias Astronómicas y Geofísicas, Universidad Nacional de La Plata, Paseo del Bosque, B1900FWA La Plata, Argentina*
[4]*Instituto de Astrofísica de La Plata (CCT-La Plata, CONICET-UNLP), Paseo del Bosque, B1900FWA La Plata, Argentina*
[5]*Departamento de Astronomía, Universidad de Concepción, Casilla 160-C, Concepción, Chile*

Accepted 2013 February 8. Received 2013 February 7; in original form 2012 September 5

ABSTRACT

We present Gemini *griz′* photometry for 521 globular cluster (GC) candidates in a 5.5 × 5.5 arcmin^2 field centred 3.8 arcmin to the south and 0.9 arcmin to the west of the centre of the giant elliptical galaxy NGC 4486. All these objects have previously published $(C - T_1)$ photometry. We also present new $(C - T_1)$ photometry for 338 globulars, within 1.7 arcmin in galactocentric radius, which have $(g - z)$ colours in the photometric system adopted by the Virgo Cluster Survey of the Advanced Camera for Surveys of the *Hubble Space Telescope* (*HST*). These photometric data are used to define a self-consistent multicolour grid (avoiding polynomial fits) and preliminarily calibrated in terms of two chemical abundance scales. The resulting multicolour colour–chemical abundance relations are used to test GC chemical abundance distributions. This is accomplished by modelling the 10 GC colour histograms that can be defined in terms of the *Cgriz′* bands. Our results suggest that the best fit to the GC observed colour histograms is consistent with a genuinely bimodal chemical abundance distribution $N_{\rm GC}(Z)$. On the other side, each ('blue' and 'red') GC subpopulation follows a distinct colour–colour relation.

Key words: galaxies: haloes – galaxies: star clusters: general.

1 INTRODUCTION

Globular clusters (GCs) are tracers of early events in the star-forming history in galaxies. However, a unique integrating picture of that history, beyond some tentative approaches, is still missing. A thorough review of several issues in this context is presented, for example, in Brodie & Strader (2006). Important aspects, that eventually deal with large-scale properties of galaxies (see, for example Forte, Vega & Faifer 2012, and references therein) are both the age and chemical abundance distribution of these clusters.

Even though the quality and volume of chemical abundance ([Z/H]) data for GCs is steadily growing (Alves-Brito et al. 2011; Usher et al. 2012), a key issue remains as an open subject: the connection between the GC abundances and their integrated colours.

Under the common assumption of old ages, GC integrated colours should be dominated by chemical abundance (and in a secondary way by age). Evidence in this sense can be found, for example, in Norris et al. (2008) and, in the particular case of elliptical galaxies, in Chies-Santos et al. (2012).

A survey of the literature reveals numerous attempts to link colours and chemical abundance, ranging from linear (Geisler & Forte 1990), quadratic (Harris & Harris 2002; Forte, Faifer & Geisler 2007; Moyano Loyola, Faifer & Forte 2010) or quartic dependences (Blakeslee, Cantielo & Peng 2010). A recent contribution on this subject has been presented by Usher et al. (2012) who adopt broken line fits.

★ Based on observations obtained at the Gemini Observatory, which is operated by the Association of Universities for Research in Astronomy, Inc., under a cooperative agreement with the NSF on behalf of the Gemini partnership: the National Science Foundation (United States), the Science and Technology Facilities Council (United Kingdom), the National Research Council (Canada), CONICYT (Chile), the Australian Research Council (Australia), Ministerio da Ciencia e Tecnologia (Brazil) and Ministerio de Ciencia, Tecnología, e Innovación Productiva (Argentina).

† E-mail: forte@fcaglp.unlp.edu.ar

A clarification of the colour–abundance connection is required, since some non-linear relations (e.g. 'inflected') can eventually lead to GC bimodal colour distributions, even when a unimodal chemical abundance distribution is assumed (see, for example, Yoon et al. 2011). Since bimodal colour distributions have often been identified as the result of genuine bimodal chemical abundance distributions, the presence of non-linearities would have important consequences on the interpretation of the GC chemical abundance distributions and also on their possible quantitative connections with the diffuse stellar population in a given galaxy.

NGC 4486 is a particularly useful galaxy in order to revise the chemical abundance-integrated colour issue due to its large GC population and relative proximity to the Sun, ≈16.6 Mpc (Tonry et al. 2001; Blakeslee et al. 2009). This paper presents Gemini *griz*′ high-quality photometry for a selected field centred 3.9 arcmin from the centre of the galaxy, including 521 GC candidates, and new $(C - T_1)$ photometry for 338 clusters within a galactocentric radius of 1.7 arcmin, which also have $(g - z)$ colours obtained with the Advanced Camera for Surveys (ACS) of the *Hubble Space Telescope* (*HST*) (Jordán et al. 2009). In addition, aiming at extending the wavelength coverage towards the ultraviolet, we combine our Gemini photometry with the *C* magnitudes (Washington system; Harris & Canterna 1977) data presented by Forte et al. (2007, hereafter FFG07). All these data sets can be, first, mutually connected to define a self consistent multicolour grid, and then calibrated in terms of different chemical abundance scales, with a final goal of obtaining a simultaneous connection between metallicity and the colour-indices grid.

The structure of the paper is as follows. Observations and data handling are presented in Section 2. The relation between the 10 colour indices defined by the *Cgriz*′ photometry is given in Section 3. This last section also explains the connection between those colour indices and others, like $(C - T_1)$, $(g - z)_{(ACS)}$, commonly used in extragalactic GCs research. Section 4 presents a preliminary calibration in terms of chemical abundance using two different empirical colour–metallicity scales: Blakeslee et al. (2010), and alternatively, the scale presented by Usher et al. (2012), that are referred to as B10 and U12, respectively, in what follows. As explained in Section 5, the multicolour grid can be used to define different magnitude curves (or pseudo-spectral distributions) as a function of [Z/H]. These *template* curves are used to clean the GC candidates photometric sample from field interlopers. The analysis of the residuals, in turn, would allow the detection of eventual age effects. The determination of GCs [Z/H], via multicolour fits, is presented in Section 6. The results of confronting the 10 observed GC colour histograms with models that adopt each chemical abundance calibration are described in Section 7. The final conclusions are given in Section 8.

2 OBSERVATIONS AND DATA HANDLING

The photometric observations presented in this paper were carried out with the Fred Gillette 8-m Telescope (Gemini north) and are part of a programme that also includes GMOS spectroscopy of a sample of selected objects that are considered as good GCs candidates (GN-2010A-Q-21; PI: J. C. Forte). The field (5.5 arcmin on a side), centred 3.8 arcmin to the south and 0.9 arcmin to the west of NGC 4486, is shown in Fig. 1. The observing log, including dates, filters, exposures, mean air mass and composite seeing [full width at half-maximum (FWHM)] is given in Table 1.

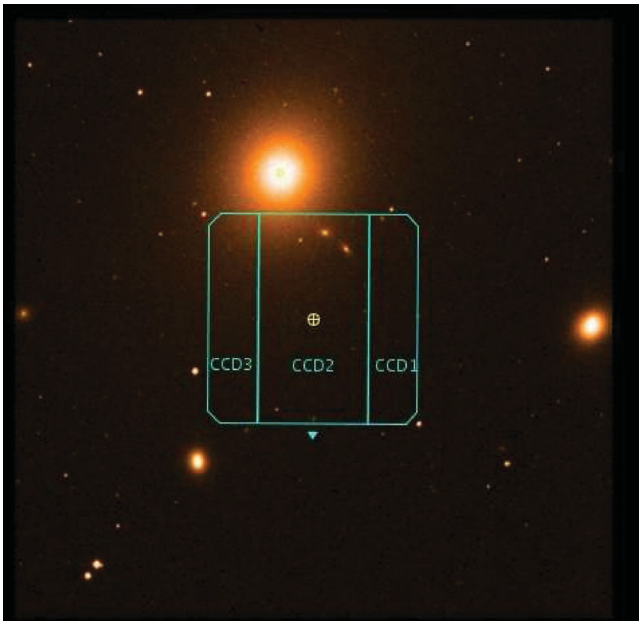

Figure 1. The GMOS field (cyan lines square; 5.5 arcmin on a side) discussed in this work. NGC 4486 appears up and to the left. North is up and east to the left.

Table 1. Observing log of Gemini-GMOS observations.

Date	Filter	Exposure (s)	Airmass	Seeing (arcsec)
2010/01/16	g'	5 × 400	1.009	0.63
2010/01/16–17	r'	5 × 300	1.017	0.60
2010/01/17	i'	5 × 300	1.147	0.54
2010/01/17	z'	6 × 450	1.080	0.47

Image processing was performed with the tasks of the package GMOS within IRAF.[1] In turn, point spread function (PSF) magnitudes were obtained with the package DAOPHOT within IRAF. These instrumental magnitudes were corrected for atmospheric extinction adopting the coefficients given in the Gemini web pages,[2] and transformed to the *griz*′ system using zero-points derived from observations of a standard field (PG1323+086), in a way similar to that extensively described in Faifer et al. (2011). The identification of GC candidates, using both DAOPHOT and SEXTRACTOR (Bertin & Arnouts 1996), also follows the lines described in that paper. The limiting magnitude of the photometric sample is $g'_0 \approx 23.7$ mag, i.e. ≈0.15 mag brighter than the turnover of the GCs integrated luminosity function (Villegas et al. 2010). The photometric errors as a function of the g' magnitudes are given in Table 2.

In what follows, we adopt a colour excess $E(B - V) = 0.02$ mag from the maps by Schlegel, Finkbeiner & Davis (1998), and the interstellar extinction relations given in Jordán et al. (2004). The magnitudes and colours, corrected for interstellar reddening (denoted with the '0' subscript), of our GC sample are given in Table 3.

[1] IRAF is distributed by the National Optical Astronomy Observatories, which are operated by the Association of Universities for Research in Astronomy, Inc., under cooperative agreement with the National Science Foundation.
[2] http://www.gemini.edu/sciops/instruments/gmos/calibration?q=node/10445

Table 2. *Cgriz′* photometry errors, in magnitudes.

g'	$\sigma_{g'}$	$\sigma_{r'}$	$\sigma_{i'}$	$\sigma_{z'}$	σ_C
20.5	0.011	0.010	0.012	0.019	0.034
21.5	0.012	0.010	0.012	0.020	0.033
22.5	0.015	0.011	0.014	0.020	0.045
23.5	0.027	0.017	0.022	0.035	0.055
24.0	0.032	0.021	0.027	0.039	0.070

Table 4. GC candidates with ACS and Washington photometry within a galactocentric radius of 100 arcsec in NGC 4486. *The full version of the table will be available in the electronic edition of the Journal.*

α (degrees)	δ (degrees)	T_{1_0} (mag)	g_0 (mag)	$(C-T_1)_0$ (mag)	$(g-z)_{0(\mathrm{ACS})}$ (mag)
187.7037354	12.3645134	22.686	23.429	1.140	0.900
187.7002411	12.3649130	22.876	23.701	0.940	0.789

The 521 GC candidates listed in Table 3 also have $(C - T_1)$ photometry obtained with the CTIO Blanco 4-m Telescope and presented in FFG07. The GCs identification numbers are from that work. Due to severe incompleteness effects, data for GCs closer to the galaxy centre were not published in FFG07. Among these objects, we identified 338 that were also observed in the ACS $(g - z)$ colour (Jordán et al. 2009). The photometric values for these GC candidates are listed in Table 4, where the RA and Dec. values come from this last work.

The distribution on the sky for objects within our Gemini field are depicted in Fig. 2, while their g'_0 versus $(g - z)'_0$ and T_{1_0} versus $(C - T_1)_0$ colour–magnitude diagrams are shown in Fig. 3.

3 MULTICOLOUR RELATIONS

The adoption of a polynomial fit to represent the dependence of integrated GC chemical abundance [Z/H] with some particular colour index (or vice versa), is a usual approach in the literature. For example, a linear fit was attempted by Geisler & Forte (1990), while two second-order polynomials, minimizing the errors in abundance or in colour, were presented by Harris & Harris (2002). In turn, both Moyano Loyola et al. (2010) and Blakeslee et al. (2010) adopted the ROBUST routine, in their respective second- and quartic-order approximations. That routine seeks minimizing the 'orthogonal' errors (defined in terms of a residual that combines those of the two variables). This approach was also adopted by Blakeslee et al. (2012), when deriving the relation between the $(g - I)$ and $(I - H)$ colours of GC candidates in the central field of NGC 1399.

In this paper, we attempt a different approach aiming at connecting simultaneously the 10 different colour indices that can be defined through the *Cgriz′* photometry and avoiding polynomial fits. The resulting self-consistent colour-grid is then tentatively calibrated in terms of two chemical abundance scales, as explained in the following section.

As a first step, we generated nine colour–colour planes, all including the $(g - z)'_0$ colour, the index with the longest wavelength base (in terms of the Gemini photometry). We preferred that index instead of $(C - z')_0$ given the larger errors inherent to the *C* magnitudes (see Table 2). Each photometric value was then convolved with a Gaussian kernel to generate bi-dimensional images that were afterwards used to obtain modal colour values. The adopted kernel size (0.05 mag) matches the overall error of the colours in our sample.

These images, generated and processed with IRAF (through the routines *irafil* and *Gaussian*), were used to determine the modal values linking each index at a given $(g - z)'_0$ colour (from 0.80 to 1.50 with 0.1 mag intervals, and adding two points at the bluest and reddest ends: 0.75 and 1.55 mag, respectively). Outside these limits the determination of the modes becomes uncertain. An example, corresponding to the $(g - r)'_0$, $(r - i)'_0$ and $(i - z)'_0$ versus $(g - z)'_0$ relations is depicted in Fig. 4.

We also performed a number of simulations starting with different types of colour–colour relations (linear, quadratic, fourth-order) and adding Gaussian errors (similar to those in Table 2). The smoothing procedure was able to recover the input relation with a typical uncertainty ranging from ±0.012 mag to ±0.02 mag. These simulations also show that changing the smoothing kernel from 0.03 to 0.08 mag has no detectable impact on the derived modal colours.

In fact, each modal colour value can be determined in four different ways. First, directly from the plane determined by a given colour versus $(g - z)'_0$ and then by properly combining all the other indices including the filter bands that define that colour (e.g., the $(C - g')_0$ versus $(g - z)'_0$ relation can also be determined from the $[(C - r')_0 - (g - r)'_0]$, $[(C - i')_0 - (g - i)'_0]$ and $[(C - z')_0 - (g - z)'_0]$ modal colour differences determined at a given $(g - z)'_0$). These four indices will differ as a result of the distinct roles played by the photometric errors on each of the two colour planes.

A check for consistency indicates that, for a given mean colour, the scatter of each four modal colours has a typical rms of ≈0.012 mag (and ≈0.018 mag in the worst case) over the whole grid. The link to the $(C - T_1)_0$ colour was obtained adopting the same method described above, i.e. by generating two smoothed colour planes and looking for the modal colour values. In turn, $(C - T_1)_0$ was also connected to $(g - z)_{0(\mathrm{ACS})}$ through the GC candidates in common with Jordán et al. (2009), listed in Table 4.

From the colour grid we derive:

$$(C - T_1)_0 = 1.25\,(\pm 0.03)\,(g - z)_{0(\mathrm{ACS})} + 0.08\,(\pm 0.04). \quad (1)$$

This equation corresponds to the formal bisector fit. We stress, however, that there is a deviation at the blue extreme that, as discussed later, seems to be a common feature in all the colour–colour relations involving the *C* filter, possibly as a consequence of the presence of the features connected with the *4000 Å break*. From the same grid, we obtain:

$$(g - z)'_0 = (g - z)_{0(\mathrm{ACS})} - 0.07\,(\pm 0.02). \quad (2)$$

Table 3. Multicolour photometry for GC candidates in the NGC 4486 field. Magnitudes and colours are corrected for interstellar extinction and reddening. Identification numbers are from Forte et al. (2007). *The full version of the table will be available in the electronic edition of the Journal.*

ID	g'_0	$(C-g')_0$	$(C-r')_0$	$(C-i')_0$	$(C-z')_0$	$(g-r)'_0$	$(g-i)'_0$	$(g-z)'_0$	$(r-i)'_0$	$(r-z)'_0$	$(i-z)'_0$	T_{1_0}	$(C-T_1)_0$
23314	22.38	0.62	1.26	1.50	1.61	0.64	0.87	0.99	0.23	0.35	0.12	21.62	1.39
23796	21.71	0.38	0.93	1.14	1.19	0.56	0.76	0.81	0.21	0.25	0.05	20.95	1.14

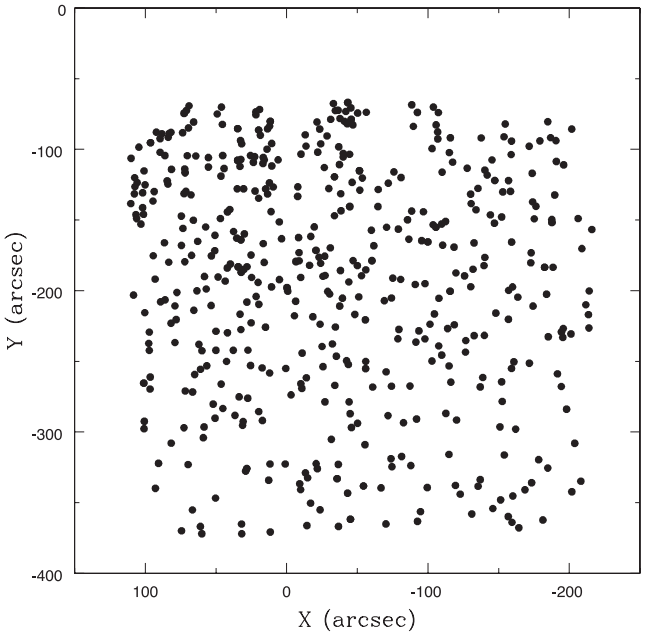

Figure 2. Distribution on the sky of 521 GC candidates with *Cgriz*′ photometry listed in Table 3. North is up, east to the left. The centre of NGC 4486 is at $x = 0.0$, $y = 0.0$.

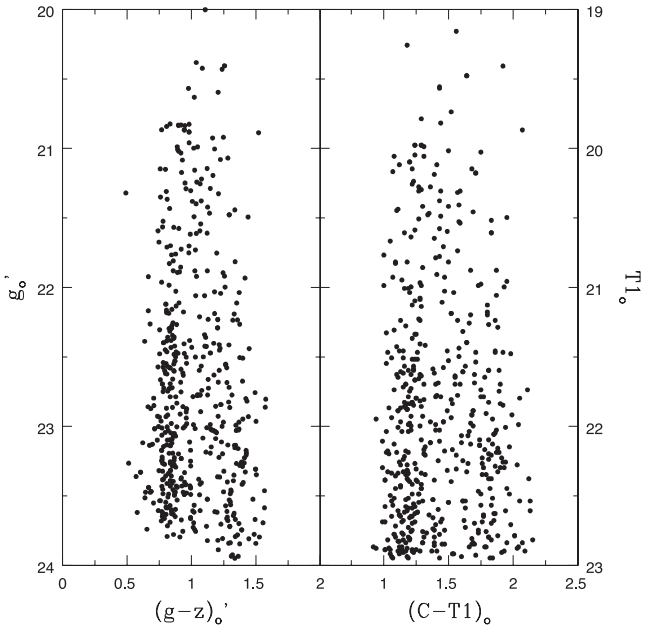

Figure 3. g'_0 versus $(g-z)'_0$ and T_{1_0} versus $(C-T_1)_0$ colour–magnitude diagrams (corrected for interstellar reddening) for the GC candidates listed in Table 3. Note incompleteness effects in the first panel for clusters bluer than $(g-z)'_0 = 1.25$.

The relations between $(C-T_1)_0$ and $(g-z)'_0$ with $(g-z)_{0(\mathrm{ACS})}$ given in Table 5 are displayed in Fig. 5.

The colour–colour relations defined by Table 5 display different degrees of non-linearity. In some cases, these effects can be noticed near the blue and red ends of the colour–colour relations. Similar kind of non-linearities were already noticed by Blakeslee et al. (2012) in their analysis of the (optical) $(g-z)_{\mathrm{ACS}}$ versus the (infrared) $(I-H)$ index. As examples, Figs 6 and 7 show the behaviour of all the colour indices defined in our photometry as a function of $(C-g')_0$ and $(g-z)'_0$, respectively.

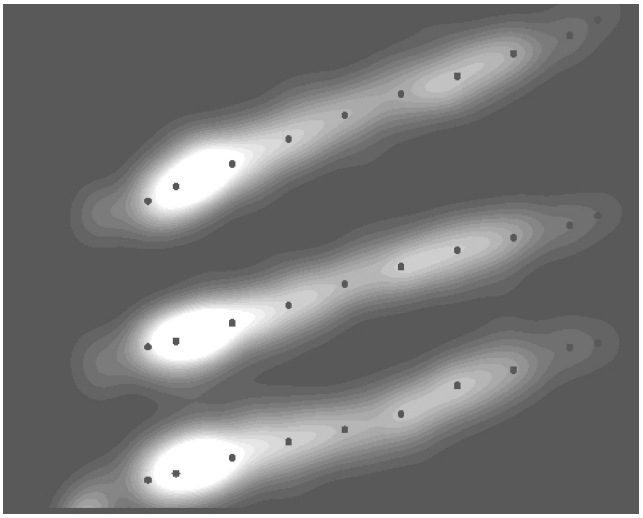

Figure 4. Smoothed colour–colour relations. From top $(g-r)'_0$, $(r-i)'_0$ and $(i-z)'_0$ (shifted arbitrarily in ordinates) versus $(g-z)'_0$. The frame is 1.1 mag on a side.

4 COLOUR–CHEMICAL ABUNDANCE RELATIONS

Despite significant effort, the shape of the relation between GC integrated colours and chemical abundance still remains a subject of debate. The main problems behind a proper determination of their relation are both the uncertainties of synthetic models and the still large errors associated with the GC chemical abundances derived, for example, via Lick indices (see Brodie & Huchra 1990).

As a preliminary approach, and in order to assess how the inferred abundances depend on the adopted calibration, we use two different empirical calibrations. On the one hand, we adopt the 'inflected' $(g-z)_{\mathrm{ACS}}$ versus [Fe/H] relation presented by B10 and, on the other, the 'broken line $(g-i)$ versus [Z/H] relation given by U12. The first one relies mostly on Galactic GCs and includes some high [Z/H] globulars from NGC 4486 and NGC 4472. In turn, the second relation stands on a compilation of the literature and spectroscopic observations of the Calcium triplet lines.

We remark that the upper abundance value given in Table 5, corresponding to the B10 calibration, is just a formal extrapolation and, in what follows (e.g. model fits), we adopt an upper cut-off at $[Z/H] = 0.40$. The same comment holds for the U12 calibration that only reaches solar abundances and is extrapolated up to $[Z/H] = 0.33$. With this caveat in mind, we note that only a small fraction of the GC candidates in our sample seem to have abundances higher than solar.

5 GLOBULAR CLUSTER CANDIDATES

In Figs 8 and 9, we display the 10 colour histograms defined in terms of the *Cgriz*′ photometry presented in this paper. These colour distributions correspond to all the objects listed in Table 3. This sample includes a fraction of field interlopers. In order to decrease the effect of these objects in our following analysis, we use the template values listed in Table 5 in an attempt to identify the genuine GCs. We stress that the rejected objects, however, have a negligible effect on the

Table 5. Multicolour–chemical abundance relations from GCs in the field of NGC 4486.

$(C-g')_0$	$(C-r')_0$	$(C-i')_0$	$(C-z')_0$	$(g-r)'_0$	$(g-i)'_0$	$(g-z)'_0$	$(r-i)'_0$	$(r-z)'_0$	$(i-z)'_0$	$(C-T_1)_0$	$(g-z)_0$ ACS	[Z/H] B10	[Z/H] U12
0.29	0.82	0.99	1.04	0.52	0.70	0.75	0.18	0.23	0.05	1.05	0.83	−2.16	−1.87
0.38	0.93	1.11	1.18	0.54	0.73	0.80	0.19	0.26	0.07	1.15	0.86	−1.88	−1.64
0.51	1.10	1.32	1.41	0.59	0.80	0.90	0.21	0.30	0.09	1.27	0.94	−1.35	−1.24
0.60	1.24	1.49	1.60	0.63	0.88	1.00	0.25	0.37	0.12	1.42	1.06	−0.84	−0.96
0.69	1.36	1.64	1.79	0.68	0.96	1.10	0.28	0.43	0.14	1.53	1.14	−0.64	−0.68
0.76	1.48	1.79	1.96	0.72	1.03	1.20	0.31	0.48	0.17	1.67	1.26	−0.44	−0.42
0.86	1.61	1.95	2.16	0.74	1.09	1.30	0.35	0.56	0.21	1.81	1.38	−0.23	−0.22
0.96	1.74	2.11	2.36	0.79	1.16	1.40	0.37	0.61	0.24	1.91	1.48	0.09	0.02
1.04	1.86	2.25	2.54	0.82	1.21	1.50	0.39	0.68	0.29	2.04	1.59	0.70:	0.19
1.08	1.92	2.33	2.63	0.85	1.25	1.55	0.40	0.70	0.30	2.11	1.64	− −	0.33

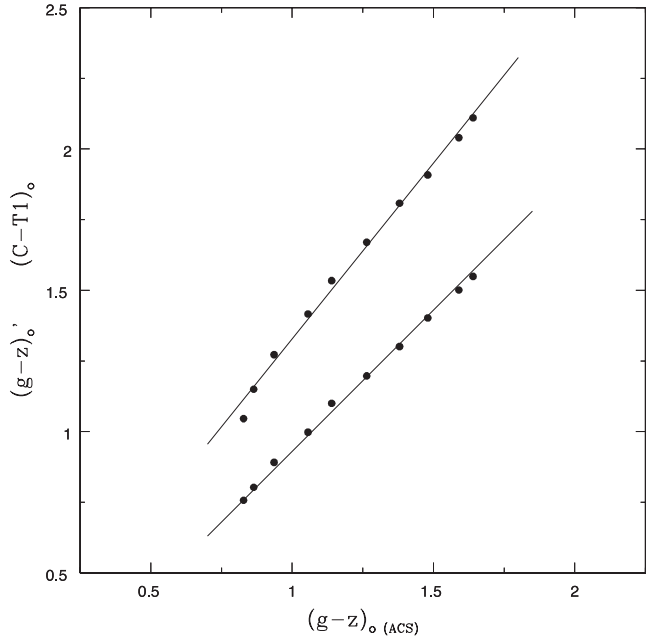

Figure 5. From top to bottom: $(C-T_1)_0$ and $(g-z)'_0$ versus $(g-z)_{0(\mathrm{ACS})}$ relations. Filled dots are the modal colours listed in Table 5. The straight lines correspond to equations (1) and (2).

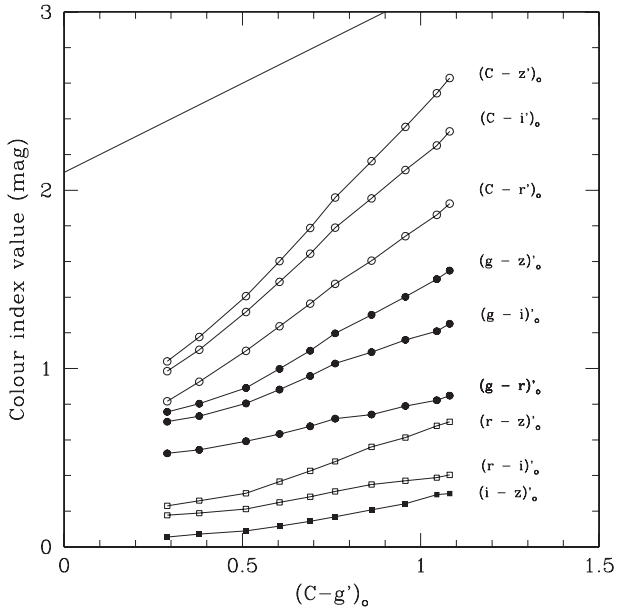

Figure 6. Colour indices versus $(C-g')_0$. From top to bottom, in decreasing order: $(C-z')_0$, $(C-i')_0$, $(C-r')_0$ *(open dots)*; $(g-z)'_0$, $(g-i)'_0$, $(g-r)'_0$ *(filled dots)*; $(r-z)'_0$, $(r-i)'_0$ *(open squares)*; $(i-z)'_0$ *(filled squares)*. The straight line at upper left has a unity slope.

definition of the modal colour–colour relations. That table defines, at each [Z/H], a template magnitude curve (or pseudo-spectral distribution) as shown in Fig. 10. In this diagram, we arbitrarily adopt a reference magnitude $z'_0 = 0.0$ mag. These curves assume that GCs are coeval on the basis of the arguments given before.

The magnitude curves were used to fit the $(Cgriz')_0$ magnitudes of all the objects listed in Table 3, i.e. we vary the [Z/H] value by interpolating in Table 5 and adopting 0.01 steps in [Z/H] until a given template curve minimizes the sum of the square residuals at each filter band. This procedure was performed using each of the chemical abundance scales.

As the results are almost identical in terms of accepted and rejected GC candidates, and for illustrative purposes, in this Section, we only show the diagrams corresponding to the adoption of the U12 calibration.

Fig. 11 shows the overall composite rms (defined by combining all the magnitude residuals) as a function of the i'_0 magnitude. We adopted this magnitude, in particular, because in this way all the photometric errors in that diagram are decoupled. The dotted line indicates an rms = 0.05 mag that we adopt as a 'reasonable' maximum acceptable value to consider a given object as a genuine GC candidate. With this criterion, the B10 scale accepts 463 objects as GC candidates and rejects 58, while the U12 scale leads to 472 and 49, respectively. The difference in the number of rejected objects arises as a consequence of the upper colour limit in the B10 calibration (see Table 5). This limit produces rms values larger than the adopted rejection limit for nine objects with colours redder than $(C-g')_0 = 0.95$, $(r-z)'_0 = 0.65$ and $(C-z')_0 = 2.5$.

The upper panel in Fig. 12 shows the residuals yielded by this procedure at each filter (characterized by their effective wavelength). These residuals do not show any systematic trend.

As a test of the effects due to an eventual range in the GC ages, we generated a Monte Carlo model that includes a spread of ±2 Gyr on top of the colour–abundance relations given in Table 5. The differential magnitude variations as a function of age were obtained using the Maraston (2005) models and adopting the 12 Gyr models as the reference age.

The output colours, including age variations but not photometric errors, were then fit with the GC templates, as in the case of the observed clusters, yielding the residuals displayed in the lower panel

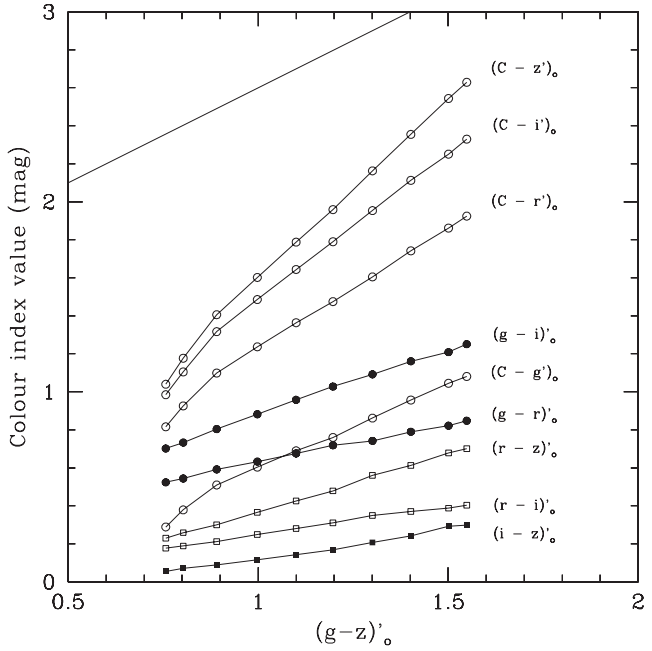

Figure 7. Colour indices versus $(g-z)'_0$. From top to bottom, in decreasing order: $(C-z')_0, (C-i)'_0, (C-r')_0, (C-g')_0$ *(open dots)*; $(g-i)'_0, (g-r)'_0$ *(filled dots)*; $(r-z)'_0, (r-i)'_0$ *(open squares)*; $(i-z)'_0$ *(filled squares)*. The straight line at upper left has a unity slope.

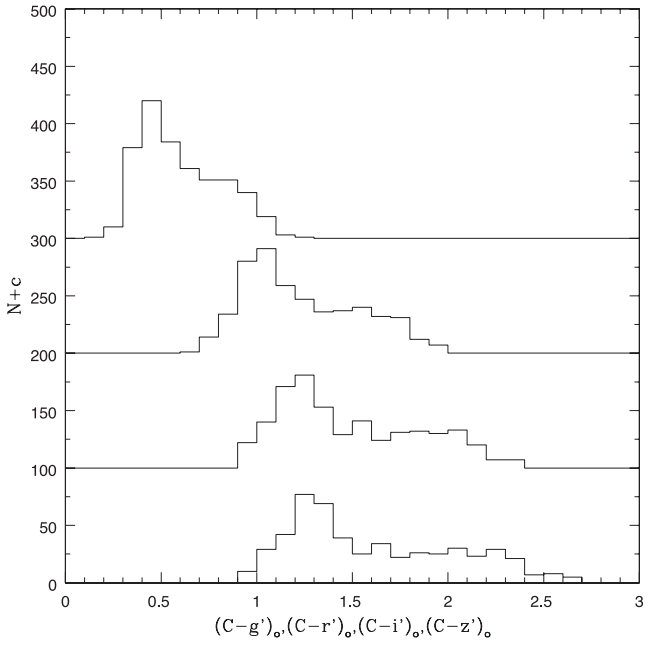

Figure 8. Colour histograms (from top to bottom): $(C-g')o$, $(C-r')o$, $(C-i')o$, $(C-z')o$ for all the objects listed in Table 3. The histograms have been shifted arbitrarily in ordinates.

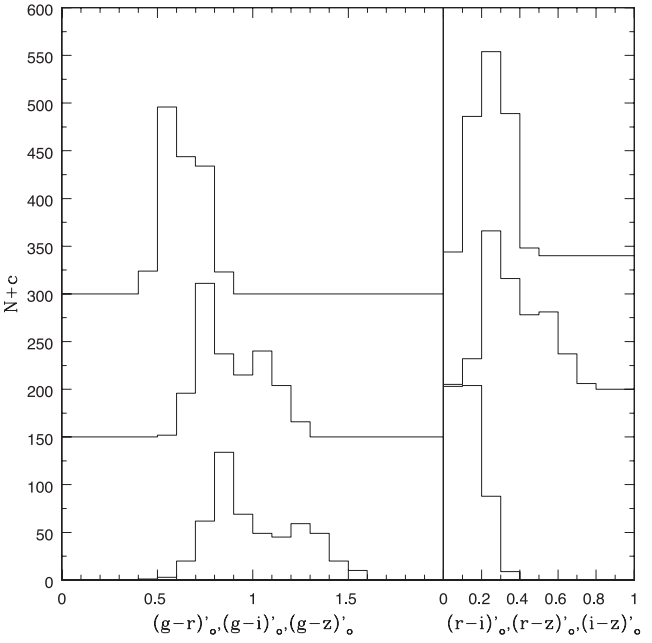

Figure 9. Colour histograms (from top to bottom, left-hand panel): $(g-r)'o$, $(g-i)'o$, $(g-z)'o$ and (right-hand panel, from top to bottom) $(r-i)'o$, $(r-z)'o$ and $(i-z)'o$ for all the objects listed in Table 3. The histograms have been shifted arbitrarily in ordinates.

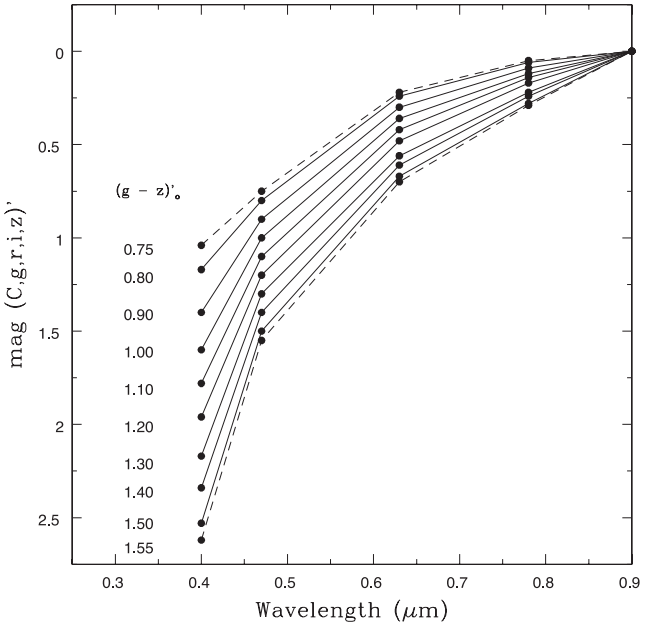

Figure 10. Magnitude curves defined by the modal colours listed in Table 5 from $(g-z)'_0 = 0.80$ to 1.50 (in 0.1 mag steps; continuous lines). The dashed upper and lower lines correspond to the extreme colours $(g-z)'_0 =$ 0.75 and 1.55, respectively.

of Fig. 12. The behaviour of these residuals indicates that age effects have no important impact on the fits as they are considerably smaller than the photometric errors. On the other hand, the same Monte Carlo models show that, with our photometric errors, the input [Z/H] values can be recovered through the magnitude curve fit with an rms ≈0.15 dex.

The number of rejected objects is consistent with previous results based on GMOS spectroscopy. In this last case, the photometric criteria adopted to define a GC candidate typically yield a contamination level of 10 per cent once these candidates are observed spectroscopically (see Faifer et al. 2011).

The residuals of the $(C-g')_0$ and $(r-z)'_0$ colours as a function of the i'_0 magnitude are shown in Fig. 13. GC candidates fainter than $i'_0 \simeq 20.5$ mag do not show obvious systematic behaviours. However, small anti-correlated trends are observed for the brightest objects.

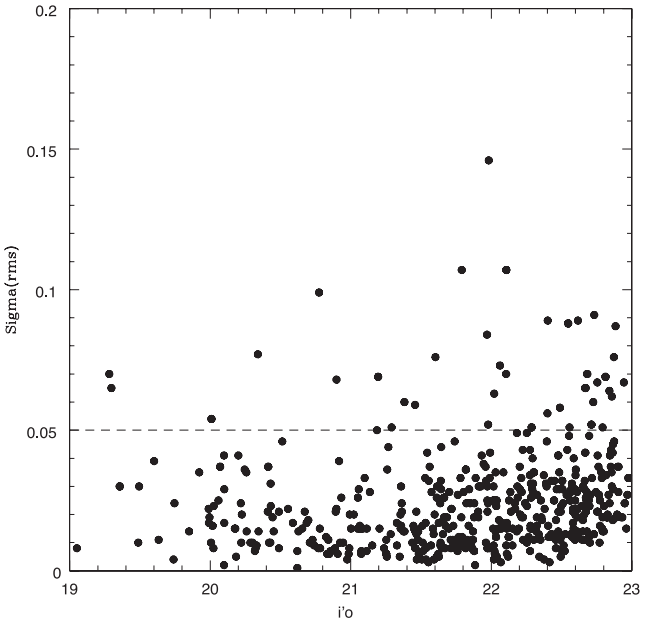

Figure 11. Root mean square values corresponding to the magnitude curve fits as a function of the i'_o magnitudes for the 521 objects included in Table 3 and adopting the U12 chemical abundance scale. Objects below 0.05 mag (dotted line) are considered as GC candidates.

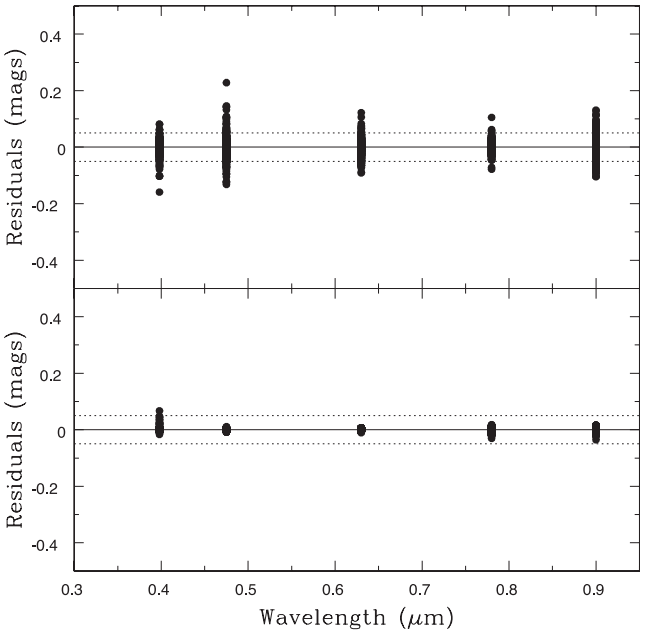

Figure 12. Upper panel: magnitude residuals (C, g', r', i', z' bands) for the whole sample (521 objects). The dashed horizontal lines indicate the adopted rms $= \pm 0.05$ mag limits that define the 'clean' GC sample. Lower panel: expected residuals from Monte Carlo modelling for an age spread of ± 2 Gyr (see the text).

We have been unable to reproduce the residual trends seen for the brightest objects just by changing the cluster ages in our models. Neither the photometric errors, nor those connected with the inferred shape of the multicolour relations, seem adequate explanations for this effect.

The clean GC sample and the rejected objects are shown in Figs 14 and 15, where we transformed $(g - z)'_0$ to $(g - z)_{0(\mathrm{ACS})}$ through equation (2). Both diagrams show non-linear behaviour with detectable changes in their slopes at $(C - g')_0 \approx 0.5$ and $(C - z')_0 \approx 1.4$, respectively. In particular, Fig. 15 can be compared with fig. 16 in Chies-Santos et al. (2011), which displays $(g - z)_{0(\mathrm{ACS})}$ as a function of the optical–infrared $(g - K)$ index for GCs in NGC 4486 and NGC 4649. Our own reading of that diagram indicates that GCs in these galaxies show changes in the colour–colour slope at $(g - K) \approx 2.90$ and $(g - K) \approx 3.5$. In turn, GCs bluer than the first

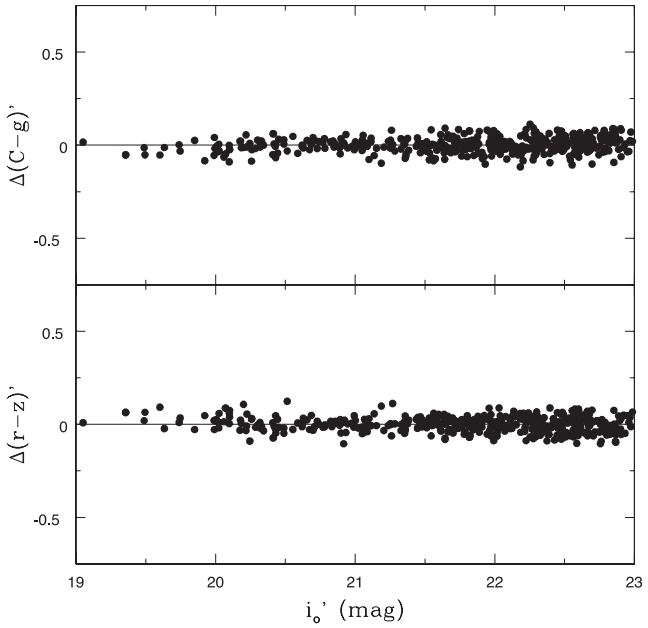

Figure 13. Fit residuals in the $(C - g)$ and $(r - z)'_0$ colours as a function of i'_0 magnitude for all the GC candidates adopting the U12 calibration.

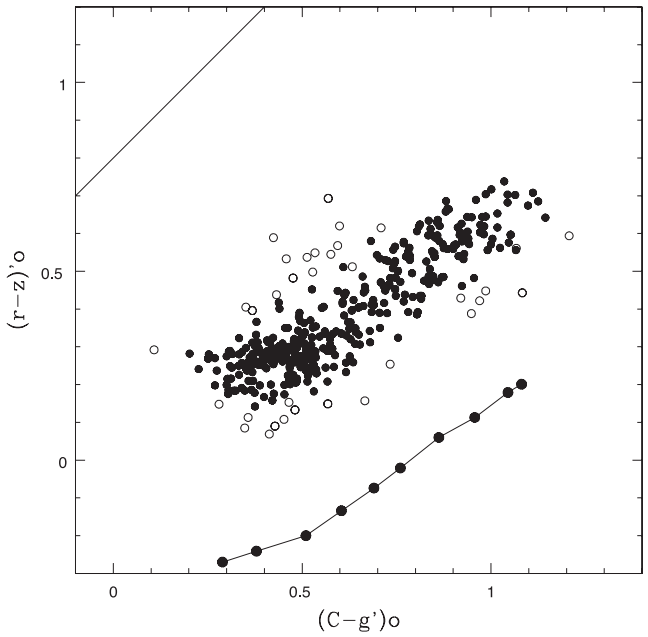

Figure 14. $(r - z)'_0$ versus $(C - g')_0$ colours showing accepted *(filled dots)* and rejected *(open dots)* GC candidates adopting the U12 calibration and after applying the rms > 0.05 mag cleaning criterion. The straight line at upper left has a unity slope. The lower curve corresponds to colours given in Table 5 shifted by -0.5 mag in $(r - z)'_0$.

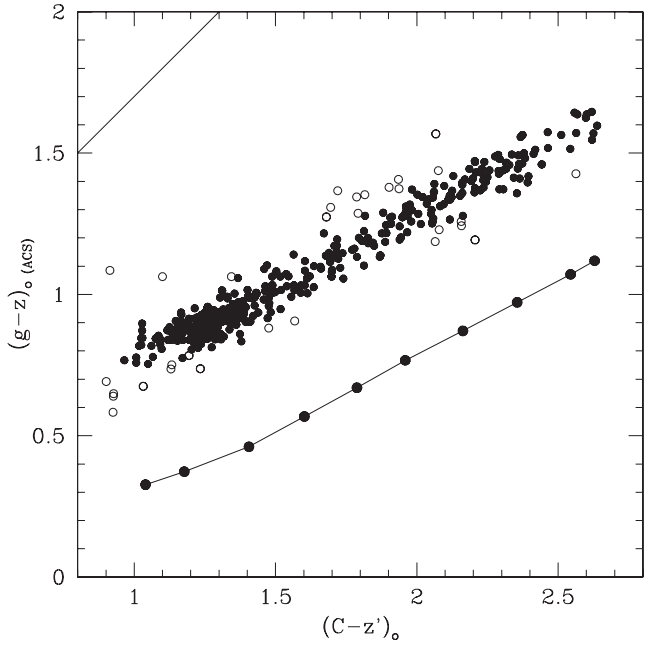

Figure 15. $(g - z)_{0(\mathrm{ACS})}$ versus $(C - z')_0$ colours for the accepted *(filled dots)* and rejected *(open dots)* GC candidates adopting the U12 calibration. The straight line at upper left has a unity slope. The lower curve corresponds to colours given in Table 5 shifted by −0.5 mag in $(g - z)_{0(\mathrm{ACS})}$.

of these colours span a $(g - z)_{\mathrm{ACS}}$ range that covers from ≈0.8 to ≈1.0, i.e. the region where we detect a change in the colour–colour slope in Fig. 15.

6 INFERRING THE GCs [Z/H] THROUGH THE TEMPLATE PSEUDO-CONTINUUMS

In this section, we make an attempt to recover the GCs [Z/H] distribution using their integrated colours. A similar approach is presented, for example, by Blakeslee et al. (2012) (see their fig. 11, right-hand panel) for the case of the NGC 1399 clusters. Instead of using a single integrated colour, in this work, we obtain the [Z/H] values for the GC candidates from the 'template-curve' fitting described in the previous section. We infer two chemical abundance distributions by alternatively adopting the B10 or U12 calibrations.

As discussed in several papers, the GC colour bimodality in NGC 4486 is better defined for GCs fainter than $T_{1_0} \approx 21.0$ mag (see, for example, FFG07 or Harris 2009) and, accordingly, we split our sample into two groups: GCs candidates with T_1 from 19.0 to 21.0 mag and T_1 from 21.0 to 23.0 mag (i.e. ∼0.2 mag brighter than the turnover of the integrated GC luminosity function).

Figs 16 and 17 exhibit the resulting [Z/H] distributions adopting the B10 and U12 calibrations, respectively and for the two GC groups. In both diagrams, the brightest clusters show distinct behaviour compared with the fainter counterparts. For the brighter GCs the abundance distributions seem broad and unimodal.

In turn, independent of the calibration, GCs fainter than $T_1 =$ 21 mag show a clear bimodality although the histograms exhibit differences in their shapes and in the position of the low and high abundance peaks (that do depend on the adopted calibration).

A simple Gaussian analysis (using the RMIX routine) indicates that, for these clusters, and for both calibrations, two Gaussian fits are strongly preferred over a single Gaussian fit, leading to χ^2 values about three to five times smaller. For the case of the B10 calibration

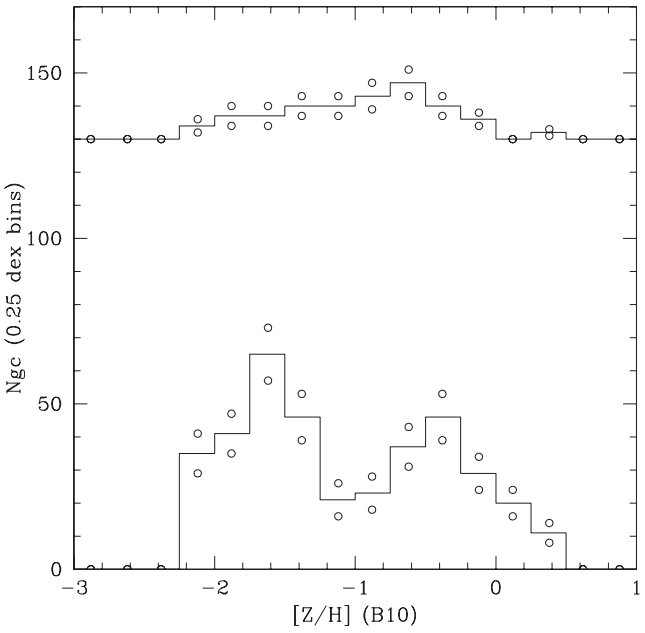

Figure 16. Inferred chemical abundance distributions adopting the B10 calibration for GC candidates brighter than $T_1 = 21.0$ mag (shifted upwards by 130 units) and for GC candidates with T_1 from 21.0 to 23 mag. Open dots correspond to the formal counting uncertainties for each bin.

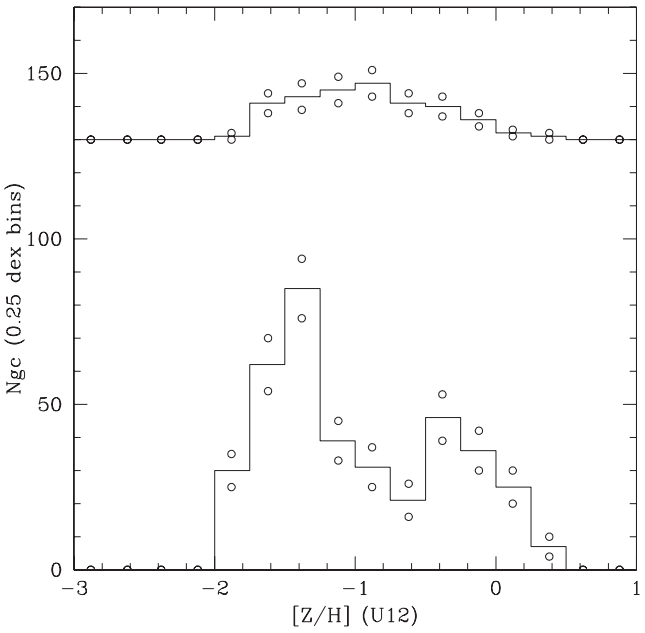

Figure 17. Inferred chemical abundance distributions adopting the U12 calibration for GC candidates brighter than $T_1 = 21.0$ mag (shifted upwards by 130 units) and for GC candidates with T_1 from 21.0 to 23 mag. Open dots correspond to the formal counting uncertainties for each bin.

($\chi^2 = 1.87$), we obtain mean [Z/H] values of −1.66 and −0.37 with dispersions of 0.32 and 0.39 dex for the blue (55 per cent of the population) and red GCs, respectively. Alternatively, adopting the U12 calibration ($\chi^2 = 0.95$), these parameters become [Z/H] of −1.42 and −0.28, with dispersions of 0.29 and 0.30 dex for the blue GCs (61 per cent of the population) and red GC populations, respectively.

As these Gaussians have comparable dispersions, we also attempted a homoscedastic KMM test that, in both cases, indicates that the probability for a single Gaussian fit to represent the [Z/H] distributions is practically null.

The situation of GCs brighter than $T_1 = 21.0$ mag is not so clear. Both the B10 and U12 calibrations lead to broad unimodal distributions that show a different degree of skewness.

The results shown in Figs 16 and 17 are different, but not necessarily in conflict, with those presented by Blakeslee et al. (2012) for the central region of NGC 1399, where red GCs are clearly the dominant subpopulation. These authors find a broad unimodal distribution with a single peak (−0.3 dex) and a tail extending towards lower chemical abundances (see their fig. 11, right-hand panel). In turn, our GCs field is located at a larger galactocentric distance, where the relative number of blue globulars is considerably larger making more evident the presence of a low-chemical abundance peak.

7 MODELLING THE GLOBULAR CLUSTER COLOUR HISTOGRAMS

Two key issues in modelling the GC colour histograms are the adopted integrated colours versus chemical abundance calibration and the assumed chemical abundance distribution of the clusters. In general, most papers have relied on a single colour–abundance calibration and also on a single GC colour histogram fit. In this work, we attempt a simultaneous fit to the 10 colour histograms that can be defined in terms of the *Cgriz′* magnitudes, adopting the (inverse) quality fit indicator χ^2, given in Côte, Marzke & West (1998). Finally, we identify the best-fitting parameters (that define the GC chemical abundance distribution) as those that yield a minimum value for the sum of the individual χ^2 indices of the 10 colour histograms (adopting the same colour bin for all the histograms: 0.10 mag).

Monte Carlo model histograms were obtained following the same procedure explained in Forte et al. (2012). First, we generate 'seed' globulars with chemical abundances Z (within the range $Z_{\rm i}$ to $Z_{\rm max}$) whose numbers are controlled by a given distribution function $N_{\rm GC}(Z)$.

After trying different simple distributions, we concluded, as in FFG07, that a double exponential dependence,

$$N_{\rm GC}(Z) \approx \exp(-Z/Z_{\rm s}), \quad (3)$$

(where $Z_{\rm s}$ is the scalelength corresponding to the blue or red GC subpopulation) is the simplest function that allows a fit to the colour histograms based on a *minimum* number of free parameters. Formally, this approach requires seven parameters: the ratio of blue to red clusters, and for each GC subpopulation the $Z_{\rm i}$ and $Z_{\rm max}$ values as well as the chemical scalelength $Z_{\rm s}$. In fact, the free parameters were reduced to five, as the minimum chemical abundance of the blue GCs subpopulation, as well as the maximum chemical abundance of the red GCs, were set as the lowest and upper values in the B10 and U12 calibrations.

The integrated colours for each GC were obtained by linear interpolation, using the logarithmic abundance as argument, in Table 5.

For each synthetic cluster, we also generate an apparent magnitude g'_0, adopting a Gaussian-integrated luminosity function and according to the parameters given by Villegas et al. (2010). These magnitudes were used as input in Table 2 in order to model (also Gaussian) observing errors that were added to each colour. Given the relatively short range in apparent magnitude, we do not include an explicit dependence of chemical abundance with brightness for the blue globulars (i.e. the 'blue tilt' effect; see, for example, Harris 2009).

Table 6. Parameters of the chemical abundance distributions giving the best overall fit to the colour histograms for Globular Clusters fainter than $T_1 = 21$.

Adopting the B10 calibration:			
$N_b = 200$	$Z_{s_b} = 0.02\,Z_\odot$	$Z_{\rm i} = 0.007\,Z_\odot$	$Z_{\rm max} = 1.0\,Z_\odot$
$N_r = 178$	$Z_{s_r} = 0.50\,Z_\odot$	$Z_{\rm i} = 0.050\,Z_\odot$	$Z_{\rm max} = 2.5\,Z_\odot$
Adopting the U12 calibration:			
$N_b = 220$	$Z_{s_b} = 0.03\,Z_\odot$	$Z_{\rm i} = 0.014\,Z_\odot$	$Z_{\rm max} = 1.0\,Z_\odot$
$N_r = 160$	$Z_{s_r} = 0.65\,Z_\odot$	$Z_{\rm i} = 0.050\,Z_\odot$	$Z_{\rm max} = 2.5\,Z_\odot$

The parameters that define the chemical abundance distributions and provide the best overall fit to the 10 colour histograms in each case, are listed in Table 6, and the corresponding individual and cumulative χ^2 indices are given in Tables 7 and 8.

Even though both models lead to $N(GC)$ values within ≈1.5 times the formal counting errors of each histogram bin, the U12 calibration yields better fits in terms of the cumulative quality index. We remark that this statement is valid only if the bi-exponential parametrization of the chemical abundance is accepted.

Each of the parameters listed in Table 6 has an associated uncertainty, which we define as the parameter variation that leads to a decrease of the fit quality, indicated by an increase of 10 per cent above the minimum total χ^2 value in the five free parameters space.

Following this, we get typical uncertainties of ± 10 GCs for each subpopulation; for the blue GCs: ± 0.01 $Z_\odot$ in Z_{sB} and ± 0.05 $Z_\odot$ in $Z_{\rm max}$; and for the red GCs: ± 0.06 $Z_\odot$ in Z_{sR} and ± 0.02 $Z_\odot$ in Z_i.

The histograms corresponding to $(C - z')_0$ colour are depicted in Figs 18 and 19. We note that this index is ≈1.6 and ≈2.0 times more sensitive to metallicity than $(C - T_1)$ and $(g - z')$, respectively. This allows the adoption of a larger colour bin (0.2 mag) thereby reducing the sampling noise. Both histograms exhibit a colour 'valley' at $(C - z')_0 \approx 1.7$, i.e. 0.3 mag redder than the colour where a change in the colour–colour relation is detectable (see Section 5). The models show that both GC populations overlap in the colour range $(C - z')_0 = 1.30-1.70$. In this range, some 20 to 25 per cent of the total number of clusters belong to the 'blue tail' of the red GC population. We note that the $(C - z')_0$ colour of the valley corresponds to $(g - z)_{0(\rm ACS)} \approx 1.1$ to 1.2, i.e. coincident with the colour region where Chies-Santos et al. (2011) claim the presence of a 'wavy feature' in the $(g - z)_{\rm ACS}$ versus $(g - K)$ relation.

The GCs [Z/H] distributions inferred from the photometric observations can be compared with those arising in the models that deliver the best fits to the 10 observed colour histograms and whose parameters are listed in Table 6.

Figs 20 and 21 display such a comparison. For clusters fainter than $T_1 = 21.0$ mag the models based on the B10 calibration yield mean [Z/H] of −1.69 and −0.47 while the adoption of the U12 calibration gives somewhat larger values, −1.46 and −0.36. These mean abundances are close to, but different from, the values arising from the simple Gaussian analysis presented before.

The fits to the brighter clusters lead to an ambiguous situation given the small number of GCs and the absence of definite peaks that prevents us from obtaining robust results.

Table 7. GC colour histograms fit χ^2 adopting the B10 calibration. First line, GCs brighter than $T_1 = 21.0$ mag; second line: GCs fainter than $T_1 = 21.0$ mag.

$(C-g)'_0$	$(C-r)_0{}'$	$(C-i)_0{}'$	$(C-z)_0{}'$	$(g-r)'_0$	$(g-i)_0{}'$	$(g-z)'_0$	$(r-i)'_0$	$(r-z)'_0$	$(i-z)'_0$	Cumulative χ^2
0.85	0.64	0.90	0.74	0.61	0.92	0.41	0.08	1.41	1.42	7.98
0.56	1.18	1.07	1.13	0.84	1.29	1.62	0.41	1.76	1.60	11.46

Table 8. GC colour histograms fit χ^2 adopting the U12 calibration. First line, GCs brighter than $T_1 = 21.0$ mag; second line: GCs fainter than $T_1 = 21.0$ mag.

$(C-g)'_0$	$(C-r)_0{}'$	$(C-i)_0{}'$	$(C-z)_0{}'$	$(g-r)'_0$	$(g-i)_0{}'$	$(g-z)'_0$	$(r-i)'_0$	$(r-z)'_0$	$(i-z)'_0$	Cumulative χ^2
0.62	0.56	0.61	0.59	0.62	0.59	0.49	0.11	0.58	0.37	5.27
0.62	0.90	0.61	0.80	1.15	0.56	0.95	0.44	0.77	0.62	7.42

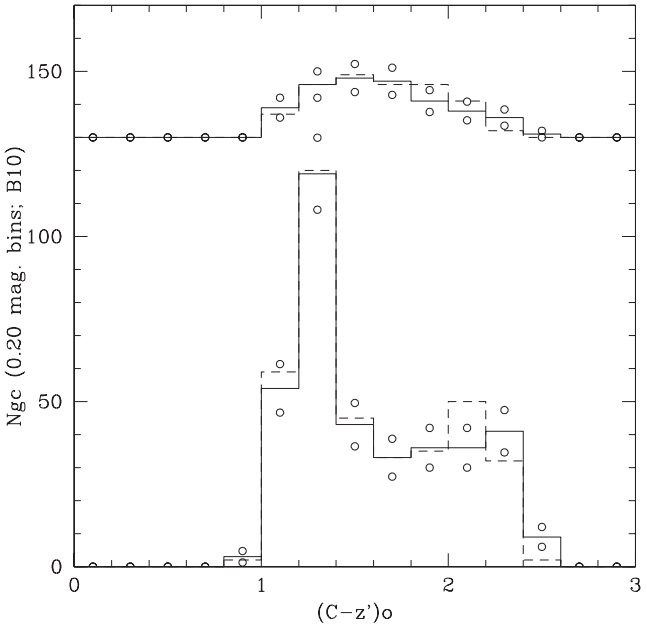

Figure 18. GC $(C - z')_0$ colour distributions adopting the B10 calibration (solid lines) for GC candidates brighter than $T_1 = 21.0$ mag (shifted upwards by 130 units) and for GC candidates with T_1 from 21.0 to 23 mag. Open dots correspond to the formal counting uncertainties for each bin. The dashed lines correspond to the best-fitting models given in Table 6.

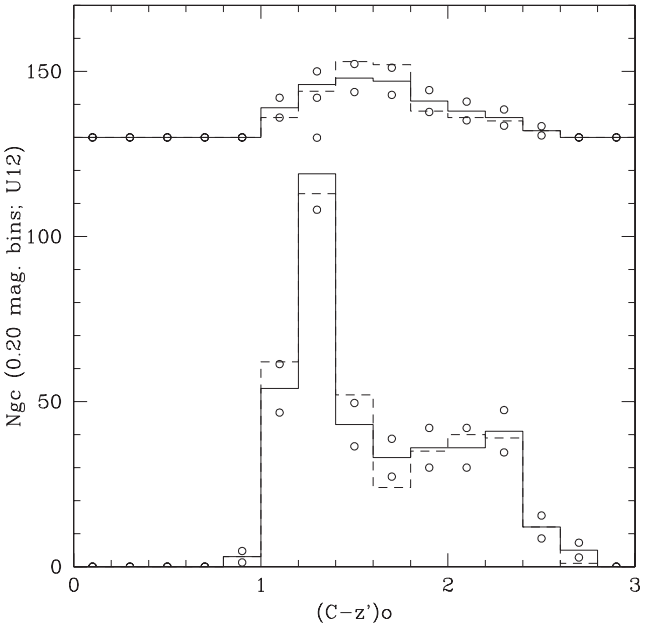

Figure 19. GC $(C - z')_0$ colour distributions adopting the U12 calibration (solid lines) for GC candidates brighter than $T_1 = 21.0$ mag (shifted upwards by 130 units) and for GC candidates with T_1 from 21.0 to 23 mag. Open dots correspond to the formal counting uncertainties for each bin. The dashed lines correspond to the best-fitting models given in Table 6.

8 CONCLUSIONS

This paper presents a self consistent multicolour *Cgriz*′ grid including 100 points, each with a typical uncertainty of $\approx\pm$ 0.012 mag, and based on GC candidates in NGC 4486. This grid, once calibrated in terms of two different colour–metallicity relations, has been used to infer the GCs chemical abundances from *Cgriz*′ photometric data and to perform a comparison with simple models.

The main results are as follows.

(1) The multicolour *Cgriz*′ relations show different degrees of non-linearities. This is more evident in those colours involving the *C* filter. Non-linearities of this kind had been previously reported by Blakeslee et al. (2012) in their study of the central regions of NGC 1399.

(2) The inferred [Z/H] distributions for GCs fainter than $T_1 = 21.0$ mag are bimodal either adopting the 'inflected' B10 or the 'broken line' U12 colour–abundance calibrations.

(3) The model fits based on a double exponential dependence of the number of clusters with chemical abundance *Z* both for the blue and red GCs provide a good representation of the GC integrated colour histograms and of their inferred chemical abundance distributions.

(4) For the brightest clusters the abundance distributions appear broad and skewed and we do not reach a definite conclusion regarding the presence of bimodality. These objects leave systematic colour residuals from the template magnitude curves that cannot be easily accounted for. In a speculative way, these residuals might indicate the presence of multistellar populations similar to those found in systems with comparable absolute magnitudes (e.g. de Boer et al. 2012).

(5) Adequate two-colour diagrams, such as $(C - g')_0$ versus $(r - z)'_0$ or $(C - z')_0$ versus $(g - z)'_0$, show changes in the colour–colour slopes. These changes are detectable, for example, at

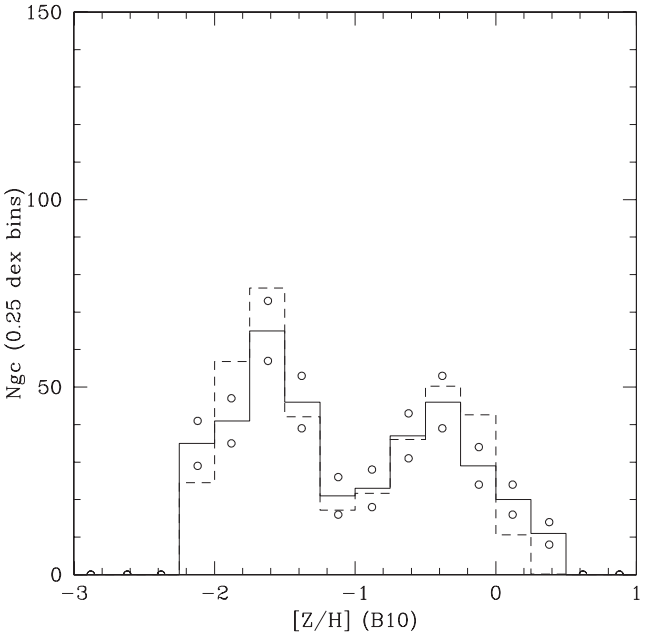

Figure 20. Comparison between the inferred [Z/H] GC distributions (solid line histogram) for GCs fainter than $T_1 = 21$ mag, and that derived from the colour histogram fits adopting the B10 calibration (dashed lines). Open dots are the formal counting uncertainties in each bin.

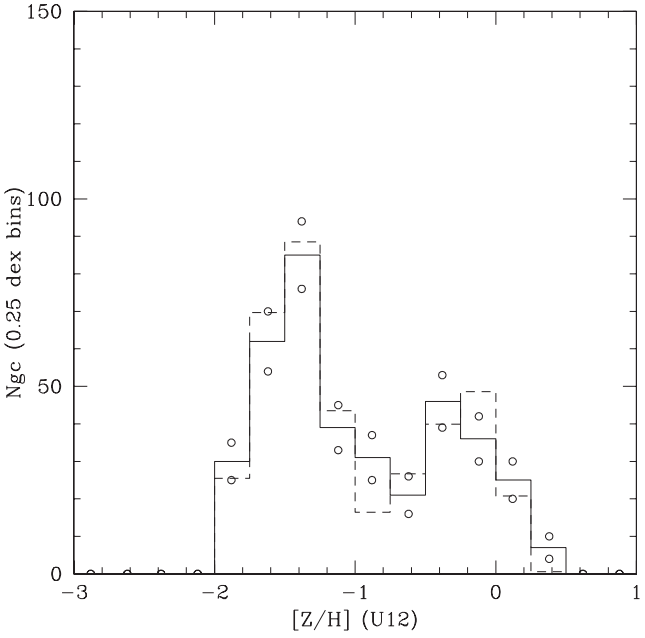

Figure 21. Comparison between the inferred [Z/H] GC distributions (solid line histogram) for GCs fainter than $T_1 = 21$ mag, and that derived from the colour histogram fits adopting the U12 calibration (dashed lines). Open dots are the formal counting uncertainties in each bin.

$(C - z')_0 = 1.4$. On the other hand, the bi-exponential modelling, adopting the B10 or U12 colour–chemical abundance relations, show that 88 and 82 per cent, respectively, of the 'blue' GCs are bluer than that colour. This indicates that the 'blue' and 'red' GC sub-populations exhibit distinct colour–colour relations with a transition zone possibly between $(C - z')_0 = 1.40$ and $(C - z')_0 = 1.60$ (where both sub-populations overlap to some degree).

The results presented in this paper suggest that the origin of the GC colour bimodality has its roots in a real bimodality of their chemical abundance distributions, and are consistent with the spectroscopic analysis of GCs in roughly half of the sample of eight galaxies studied by U12 and also by Brodie et al. (2012) in NGC 3115.

ACKNOWLEDGEMENTS

JCF acknowledges Prof. Lucía Sendón (Director) and the staff of the Planetario 'Galileo Galilei' (Buenos Aires) for their hospitality. We also thank the Referee, Dr. John Blakeslee, for careful reading and comments that improved the original version.

AVSC acknowledges financial support from Agencia de Promoción Científica y Tecnológica of Argentina (BID AR PICT 2010-0410). This work was supported by grants from La Plata National University, Agencia Nacional de Promoción Científica y Tecnológica, and CONICET (PIP-200801-1611 and PIP-2009-0712), Argentina. D.G. gratefully acknowledges support from the Chilean BASAL Centro de Excelencia en Astrofísica y Tecnologías Afines (CATA) grant PFB-06/2007.

REFERENCES

Alves-Brito A., Hau G. K. T., Forbes D. A., Spitler L. R., Strader J., Brodie J. P., Rhode K. L., 2011, MNRAS, 417, 1823
Bertin E., Arnouts S., 1996, A&AS, 117, 393
Blakeslee J. P. et al., 2009, ApJ, 694, 556
Blakeslee J. P., Cantiello M., Peng E. W., 2010, ApJ, 710, 51
Blakeslee J. P., Cho H., Peng E. W., Ferrarese L., Jordan A., Martel A. R., 2012, ApJ, 746, 88
Brodie J. P., Huchra J., 1990, ApJ, 362, 503
Brodie J. P., Strader J., 2006, ARA&A, 44, 193
Brodie J. P., Usher Ch., Conroy Ch., Strader J., Arnold J. A., Forbes D. A., Romanowsky A. J., 2012, ApJ, 759, 33
Chies-Santos A. L., Larsen S. S., Kuntschner H., Anders P., Wehner E. M., Strader J., Brodie J. P., Santos J. F. C. Jr, 2011, A&A, 525, A20
Chies-Santos A. L., Larsen S. S., Cantiello M., Strader J., Kuntschner H., Wehner E. M., Brodie J. P., 2012, A&A, 539, A54
Côte P., Marzke R. O., West M. J., 1998, ApJ, 501, 554
de Boer T. J. L. et al., 2012, A&A, 539, A103
Faifer F. R. et al., 2011, MNRAS, 416, 155
Forte J. C., Faifer F., Geisler D., 2007, MNRAS, 382, 1947 (FFG07)
Forte J. C., Vega E. I., Faifer F., 2012, MNRAS, 421, 635
Geisler D., Forte J. C., 1990, ApJ, 350, L5
Harris W., 2009, ApJ, 703, 939
Harris H., Canterna R., 1977, AJ, 82, 798
Harris W. E., Harris G. L. H., 2002, AJ, 123, 3108
Jordán A. et al., 2004, ApJS, 154, 509
Jordán A. et al., 2009, ApJS, 180, 54
Maraston C., 2005, MNRAS, 362, 799
Moyano Loyola G., Faifer F., Forte J. C., 2010, BAAA, 53, 133
Norris M. et al., 2008, MNRAS, 385, 40
Schlegel D. J., Finkbeiner D. P., Davis M., 1998, ApJ, 500, 525
Tonry J. L., Dressler A., Blakeslee J. P., Ajhar E. A., Fletcher A. B., Luppino G. A., Metzger M. R., Moore C. B., 2001, ApJ, 546, 681
Usher C., Forbes D., Brodie J. P., Foster C., Spitler L. R., Arnold J. A., Romanowsky A. J., Pota V., 2012, MNRAS, 426, 1475
Villegas D. et al., 2010, ApJ, 717, 603
Yoon S.-J. et al., 2011, ApJ, 743, 150

SUPPORTING INFORMATION

Additional Supporting Information may be found in the online version of this article:

Table 3. Multicolour photometry for GC candidates in the NGC 4486 field. Magnitudes and colours are corrected for interstellar extinction and reddening. Identification numbers are from Forte et al. (2007).

Table 4. GC candidates with ACS and Washington photometry within a galactocentric radius of 100 arcsec in NGC 4486. (http://mnras.oxfordjournals.org/lookup/suppl/doi:10.1093/mnras/stt263/-/DC1).

This paper has been typeset from a TEX/LATEX file prepared by the author.